Murray, J.W. and Algodi, Samer J. and Fay, Mike W. and Brown, Paul D. and Clare, Adam T. (2016) Formation mechanism of electrical discharge TiC-Fe composite coatings. Journal of Materials Processing Technology, 243 . pp. 143-151. ISSN 0924-0136

Formation mechanism of electrical discharge TiC-Fe composite coatings

J.W. Murray[a], S.J. Algodi[a], M.W. Fay[b], P.D. Brown[a], A.T. Clare[a,*]

[a] *Department of Mechanical, Materials & Manufacturing Engineering, Faculty of Engineering, University of Nottingham, University Park, Nottingham, NG7 2RD, UK*
[b] *Nanoscale and Microscale Research Centre, University of Nottingham, University Park, Nottingham, NG7 2RD, UK*

ABSTRACT

Comparison of electric discharge (ED) processed single deposit and continuum TiC-Fe cermet coatings, formed from a sacrificial powder metallurgy TiC tool electrode at negative polarity, on 304 stainless steel, provided insight into the ED coating (EDC) formation mechanism. A deposit from a single spark event was dominated by TiC, phase separated from a ~2 wt% Fe matrix, with strongly aligned grains and banded microstructure, indicative of solidification from the coating/substrate interface. Conversely, a continuum coating, subjected to ~200 spark events per location, exhibited a more complex, banded microstructure, with a mixture of equiaxed and columnar TiC grains within a ~30 wt% Fe-based matrix, along with some concentrations of carbon from the oil dielectric. It is considered that each sparking event remelts previously solidified coating material, with or without further TiC particle incorporation, leading to gradual TiC dilution and the development of a TiC-Fe composite coating with increasing levels of substrate material forming the matrix.

1. Introduction

Electrical discharge coating (EDC) is a surface modification process used to produce coatings from tool electrodes, and/or powder suspended in a dielectric fluid, onto a target workpiece. The EDC process exploits the principle of sparking, being an adaptation of electrical discharge machining (EDM), to deposit functionally significant amounts of material on to complex shapes and uneven surfaces, as part of an integrated manufacturing process. The use of negative tool polarity acts to promote material deposition. The high temperatures associated with sparking allow a large range of difficult to process materials, including ceramics, to be deposited, whilst rapid quenching facilitates the production of very hard coatings (Moro et al., 2004).

The performance of coatings produced by EDC is dependent on the fine-scale microstructure and elemental distribution within the layer. The EDC process is thought to involve a complex mechanism of localised melting, on the scale of an individual discharge, of the workpiece along with material removal, material deposition from the tool electrode and intermixing within the near surface of the workpiece. Functional coatings are formed then by the repetition of thousands or millions of individual discharges, depending on the total area of coverage. In this context, there is need for detailed microstructural investigations of EDC coatings, to gain improved understanding of electrical discharge coating formation mechanisms at the fundamental level.

Here, we consider candidate models for the EDC process with reference to a TiC-based coating on 304 stainless steel substrates, investigated primarily by cross-sectional transmission electron microscopy (TEM). In particular, a section taken from a localised deposit produced by a single discharge from a TiC electrode is compared with a section from a continuous coating after 30 min of processing (equating to 500 μm of tool electrode wear). Sample microstructures were characterised using the combined techniques of TEM diffraction contrast imaging, selected area electron diffraction (SAED) and energy dispersive X-ray spectroscopy (EDS), in addition to X-ray diffractometry (XRD).

1.1. Principles of EDM and EDC

The electrical discharges (plasmas) employed during EDM and EDC are fundamentally the same, but are generated with reversed

---

* Corresponding author at: A49 Coates, University Park, Nottingham, NG7 2RD, UK.

E-mail addresses: james.murray@nottingham.ac.uk (J.W. Murray), samer.algodi@nottingham.ac.uk (S.J. Algodi), michael.fay@nottingham.ac.uk (M.W. Fay), paul.brown@nottingham.ac.uk (P.D. Brown), adam.clare@nottingham.ac.uk (A.T. Clare).

polarity. EDM, as used for sinking machining, is typically characterised by an anodic tool electrode and cathodic workpiece, whilst EDC, as used for coating, employs a cathodic tool electrode and an anodic workpiece. This polarity change, combined with optimised process parameters and the high melting points of the sacrificial tool electrode materials, provides for maximised incorporation of material from the tool electrode with the workpiece.

With regard to the fundamental phenomena associated with electrical discharge (ED) processing (Kunieda et al., 2005): A voltage is established across the tool electrode and workpiece, and the generated electric field causes free electrons between the two electrodes, which are created constantly and randomly, to accelerate and collide with neutral species within the gap, in turn creating ions and more free electrons which further ionise atoms in an avalanche cascade process until a discharge plasma (spark) is fully established. At this point, the voltage drops due to the decreased electrical resistance of the plasma which is now sustained by electron emission from the cathode. The energy delivered to both electrodes causes the localised melting of material in contact with the plasma channel. Material at both electrodes becomes superheated to form a melt pool, whilst boiling is suppressed due to the high pressure exerted from the plasma. Ejection of molten material from the melt pools is thought to occur at the end of the discharge, promoted by a rapid drop in pressure (Schumacher, 2004).

The distribution of energy between the electrodes, and hence the size of resulting melt pools, depends on the discharge duration (pulse-on time) and polarity. During arc discharge, the current is sustained by a combination of thermionic and field emission from the cathode. The distribution of energy to the anode and cathode for such ED processes has been estimated at ~40% and ~25%, respectively, via the measurement of electrode temperature (Kunieda et al., 2005), with the balance of energy being used for the initiation of electrical breakdown, or lost to the dielectric medium, in our case a hydrocarbon-based oil.

The mechanism of material transfer between electrodes during ED processes is not well understood, nor is the process of coating development. Suzuki & Kobayashi showed that TiC can be supplied directly to the opposite electrode during a single discharge and that the amount of deposition is correlated with a temporary voltage drop during discharge on-time, (Suzuki and Kobayashi, 2013), however the development of the TiC-based layer itself still needs to be elucidated. The transfer of material between tool electrode and workpiece has been reported for conventional EDM for a variety of processing parameters (Kumar Saxena et al., 2016), with workpiece material becoming deposited on the positive tool electrode (Murray et al., 2012), whilst only small amounts of anode material are found within the cathode workpiece recast layer (Murray et al., 2013), consistent with the machining nature of the EDM process. However, for ED processes in a hydrocarbon-based dielectric oil, it is recognised that material removal per pulse is inhibited by the deposition of carbon on the anode (Kunieda and Kobayashi, 2004). Indeed, this carbon layer effect is the main reason for use of a tool electrode with positive polarity during conventional EDM. Hence, for the case of EDC, the sacrificial tool electrode is established with a negative polarity because it is desirable for material removal from the tool to be enhanced and not inhibited by the build-up of carbon.

Generalised descriptions of ED processes, for example summarised by (Kunieda et al., 2005) and (Schumacher, 2004), suggest also that when an electrical discharge has ended, materials from the melt pools on both tool electrode and workpiece are released into the discharge gap. At this point, there are a number of candidate pathways for materials transport to the melt pools, followed by intermixing and the solidification of individual deposits which then constitute the building blocks of a continuum coating. Based on current understanding of ED phenomena, schematic representations of possible routes for materials transport to the workpiece during

Table 1
EDC process parameters for both (a) single spark and (b) 30 min of processing.

Workpiece material	304 stainless steel
Oil (dielectric)	Shell Paraol 250
Tool electrode polarity	Negative
Process parameters	320 V; 10 A current; 8 μs ON/256 μs OFF

EDC are presented in Fig. 1, recognising that little is known about the nature of each localised melt pool during, and the resultant recast structure after, each discharge.

Fig. 1 represents candidate mechanisms for the EDC process involving repeated liberation of material from the tool electrode, and to a lesser extent the workpiece, during sequential sparking, with many repetitions leading to the build-up of a continuum layer. In the case of Fig. 1a, an initial spark leads to the ejection of particles into the dielectric oil, which act to lower the breakdown voltage and promote a subsequent spark in that location, in turn directing the particles in the oil to the workpiece surface where they merge with the associated melt pool. Fig. 1b illustrates a related mechanism, whereby material is transferred to the workpiece and fuses with the associated melt pool, as a consequence of a single discharge event. Indeed, the analysis of individual discharge craters has shown that deposition of material from tool electrode to workpiece can occur following a single discharge (Suzuki and Kobayashi, 2013). Fig. 1c relates to a spark event in the vicinity of a liberated particle already attached to the target workpiece, followed by melting and fusing with the associated melt pool.

The development of the EDC processing technique is presently limited by a lack of detailed understanding of the compositions and structures of the resultant coatings. In this context, we report on a cross-sectional TEM investigation of a TiC-Fe cermet coating produced from a TiC tool electrode formed on a 304 stainless steel substrate using standard EDC processing parameters. 304 stainless steel is used commonly across a range of engineering applications and provides an appropriate template for the appraisal of EDC processing phenomena. Comparison is made with a deposit created by a single pulse discharge, under identical processing conditions, in order to gain insight into the melt pool and solidification processes leading to coating formation.

2. Experimental

304 stainless steel substrates were prepared by grinding and sequential mechanical polishing, down to 1 μm diamond grit, to give a mirror finish prior to surface processing (*Sa* roughness ~ 0.11 μm). A Mitsubishi EA12V EDM machine was used for both single spark and continuum coating experiments, using the same processing parameters, as summarised in Table 1. The process parameters for the samples reported on here were chosen following a wider process mapping investigation of TiC-Fe based cermet coatings, to ensure the development of a surface modified layer with appropriate thickness and TiC content for practical applications, appropriate for TEM investigation. Voltage and current waveforms were recorded to validate the calibration of the EDM machine.

Samples were prepared for investigation in both plan-view and cross-sectional geometries. Hitachi S2600N and FEI XL30 scanning electron microscopes in secondary electron (SE) and backscattered electron (BSE) imaging modes were used to appraise sample topographies, whilst energy-dispersive X-ray spectroscopy (EDS) was performed using an Oxford Instruments INCA X-ray microanalysis system (20 kV; working distance 10 mm) in order to appraise sample compositions. The open-source, image processing software ImageJ was used for the measurement of layer thicknesses from cross-sectional optical microscope images, with average layer thicknesses being determined from 100 points of regular spacing
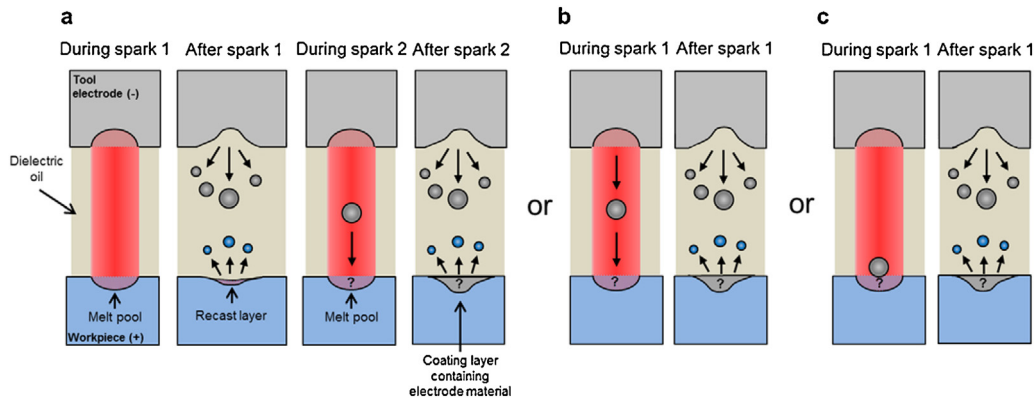
Fig. 1. Schematic representations of the EDC process, showing candidate mechanisms for material transport to the workpiece: (a) Initial spark and ejection of particles into the dielectric fluid which are then directed to the workpiece surface and merge with the melt pool induced by the next spark; (b) Material transferred directly to the workpiece during a single discharge event; (c) Particle on the workpiece surface promoting a favourable pathway for localised discharge, leading to particle melting and incorporation into the melt pool.

along a 10 μm length of the coating. Crystal structures were investigated by X-ray diffractometry (XRD) using a Bruker AXS D500 in conventional θ/2θ geometry (Cu k_α (λ = 1.54060 Å); 40 kV; 25 mA; 0.02° step size; 8 s per step). Site-specific single deposit and continuum coating samples for cross-sectional transmission electron microscopy (TEM) investigation using a JEOL 2100F operated at 200 kV were prepared using an FEI Quanta 200 3D focused ion beam SEM (FIBSEM) operated at 30 kV. Transfer of electron transparent membranes to TEM support grids was achieved using an Omniprobe in-situ nanomanipulator.

3. Results

3.1. Morphology of TiC-Fe cermet coated 304 stainless steel

The SE image of Fig. 2a is typical of a TiC-based continuum coating on a 304 stainless steel substrate, following 30 min of EDC processing (corresponding to ~500 μm of tool electrode wear). In particular, cracking was prevalent with a cellular distribution, consistent with the size and distribution of individual discharge craters. The complementary optical microscope image of Fig. 2b shows the sample in cross-sectional geometry and demonstrates a significant variation in layer thickness, with mean value ~8 μm (Fig. 2c).

The crystal structures of an as-polished 304 stainless steel substrate, a starting TiC tool electrode and a continuum TiC-Fe coating, as processed by EDC, were investigated using XRD (Fig. 3a–c). The XRD data set covers 2θ = 34°–52°, since no additional phases were revealed beyond this value range.

The as-polished substrate was dominated by peaks due to austenite, along with some small peaks attributable to martensite/ferrite (Fig. 3a). The tool electrode was characterised simply by peaks attributable to TiC (Fig. 3b). The XRD pattern from the coating was dominated by TiC along with comparable peaks due to austenite and martensite (Fig. 3c). A change in the ratio of peak heights for the TiC suggested a level of preferred orientation for the coating, as compared to the powder metallurgy (PM) tool electrode material which was equiaxed. Minor peaks, attributed to Fe_3C and Cr_3C_2 were detected also.

Fig. 4a presents a bright field TEM image showing the near surface grain structure of the continuum TiC-Fe coating in cross-section, with boxed regions, magnified in the dark field-TEM images in Fig. 4b and c, showing a band (~1 μm deep) of fine scale (<50 nm) equiaxed grains towards the surface; a transition zone with slightly larger grains (100–200 nm) interspersed with carbon deposits; then a region of grains showing distinct columnar growth. Fig. 4d–f present complementary low and high magnification annular dark field (ADF) STEM images of this sample with associated EDS maps, showing that the layer was indeed a metal matrix ceramic composite containing a dispersion of TiC and Fe, consistent with the XRD data, along with some patches of carbon.

Fig. 4f presents representative Convergent Beam Electron Diffraction (CBED) patterns from grains near to the coating surface with: (1,2) patterns acquired from a cluster of TiC grains in the same crystallographic orientation; (3,4) patterns corresponding to an Fe-based matrix phase, also in an single crystallographic orientation; (e.g. 5) pattern acquired from a small, randomly oriented TiC grain close to the top surface; and (e.g. 6) pattern acquired from an amorphous patch, attributable to carbon. The CBED patterns (Fig. 4f:1–6), recorded with a highly converged probe, were used simply to establish which of the grains were crystalline or amorphous, with the composition of grains being established as TiC, ferrite/martensite or C, as appropriate, using EDS.

Table 2 summarises the elemental composition of the area shown in Fig. 4f, as compared with that of the stainless steel substrate, consistent with the development of a complex intermixture of workpiece and tool electrode elements, whilst the chemical maps of Figs. 4d,e confirm a distribution of distinct TiC grains within an Fe-based matrix, confirming again that the developed coating is indeed a cermet. Further, the EDS maps indicated that carbon was fairly well distributed uniformly throughout the crystalline regions of the coating, along with enhanced concentrations attributable to amorphous, inter-granular carbon (Fig. 4f, arrowed). The data is consistent also with the presence of some martensite, as distinct from ferrite, as a result of the rapid quenching of austenite, again in accordance with the XRD data.

3.2. Morphology of a single discharge deposit

Fig. 5a,b present complementary SE and BSE images of localised craters and deposits on a 304 stainless steel substrate EDC processed for 30 s. The BSE image of Fig. 5b, in particular, reveals compositional variations with dark regions corresponding to material with low, locally averaged atomic number, commensurate with the presence of localised tool electrode TiC deposits within the stainless steel. The effects of many discharges which did not result in deposition in the vicinity of this deposit can be seen also, in the form of craters exhibiting similar BSE brightness levels to that of the substrate (Fig. 5b, arrowed).

Fig. 5c shows the location selected for FIB lift-out, corresponding to the deposit highlighted within the boxed region of Fig. 5b. The site was coated with a protective layer of Pt, via the FEI Pt gas injection system, prior to FIB milling using Ga$^+$ ions at 30 kV,
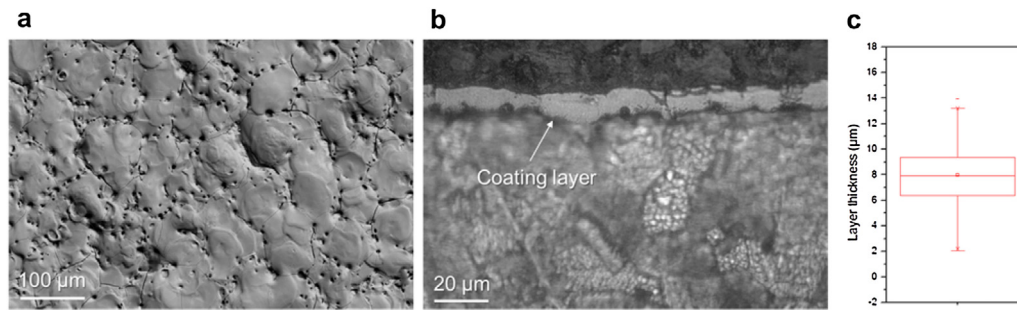
Fig. 2. (a) SE image of TiC-based cermet coating on 304 stainless steel following 30 min of EDC processing; (b) Complementary optical microscope image of coating in cross-section geometry; and (c) Box plot of layer thickness resulting from 100 measurements (mean value ∼ 8 μm).
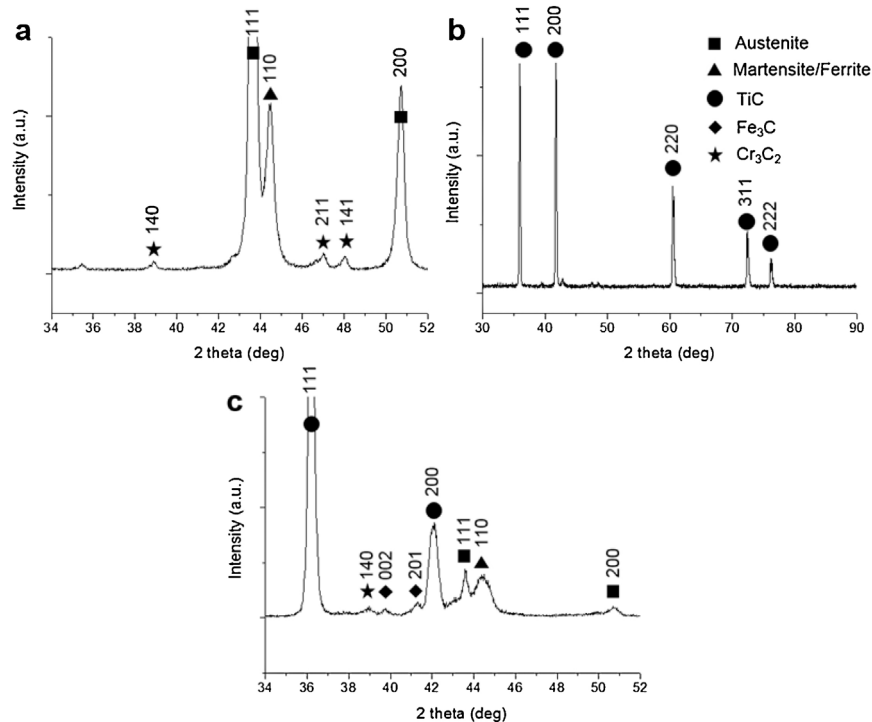

Fig. 3. XRD patterns of: (a) an as-polished 304 stainless steel substrate; (b) a TiC tool electrode; and (c) a continuum TiC-Fe cermet coating.

Table 2
EDS data from region shown in Fig. 4f, as compared with the stainless steel substrate.

Element/wt%	C	Si	Ti	Cr	Mn	Fe	Ni	Pt
Region 4f	12.88	0.17	39.37	9.08	0.68	29.70	2.78	5.34
Substrate	7.22	0.40	–	16.96	1.69	66.44	7.28	–

Table 3
EDS data from boxed regions *i–iii* shown in Fig. 6a confirming the dominance of TiC within this deposit.

wt%								
	C	Ti	Cr	Fe	Cu	Ga	Pt	Au
i	34.40	45.32	0.54	1.90	15.27	0.67	1.10	0.81
ii	23.51	57.98	0.18	0.01	15.46	0.93	1.39	0.53
iii	29.13	53.03	0.12	0.68	15.02	0.31	0.64	1.07

with sequential reduction of ion beam current density to define an electron transparent membrane (∼10 × 6 μm), free of surface amorphisation artefacts, for observation in cross-section in the TEM. A sub-section of the TEM lamella, ∼3 μm wide, was ion beam polished to <100 nm thickness for improved electron transparency.

Fig. 6a presents a BF-STEM image of this deposit showing the presence of three distinct bands of material; *i.e.* a near surface region *(i)* of 50–200 nm sized grains with slight preferred orientation; a thicker banded region *(ii)* of much larger ∼1–2 μm sized grains; then a narrow transition zone of small, 50–200 nm sized equiaxed grains into a further distribution *(iii)* of ∼1 μm long
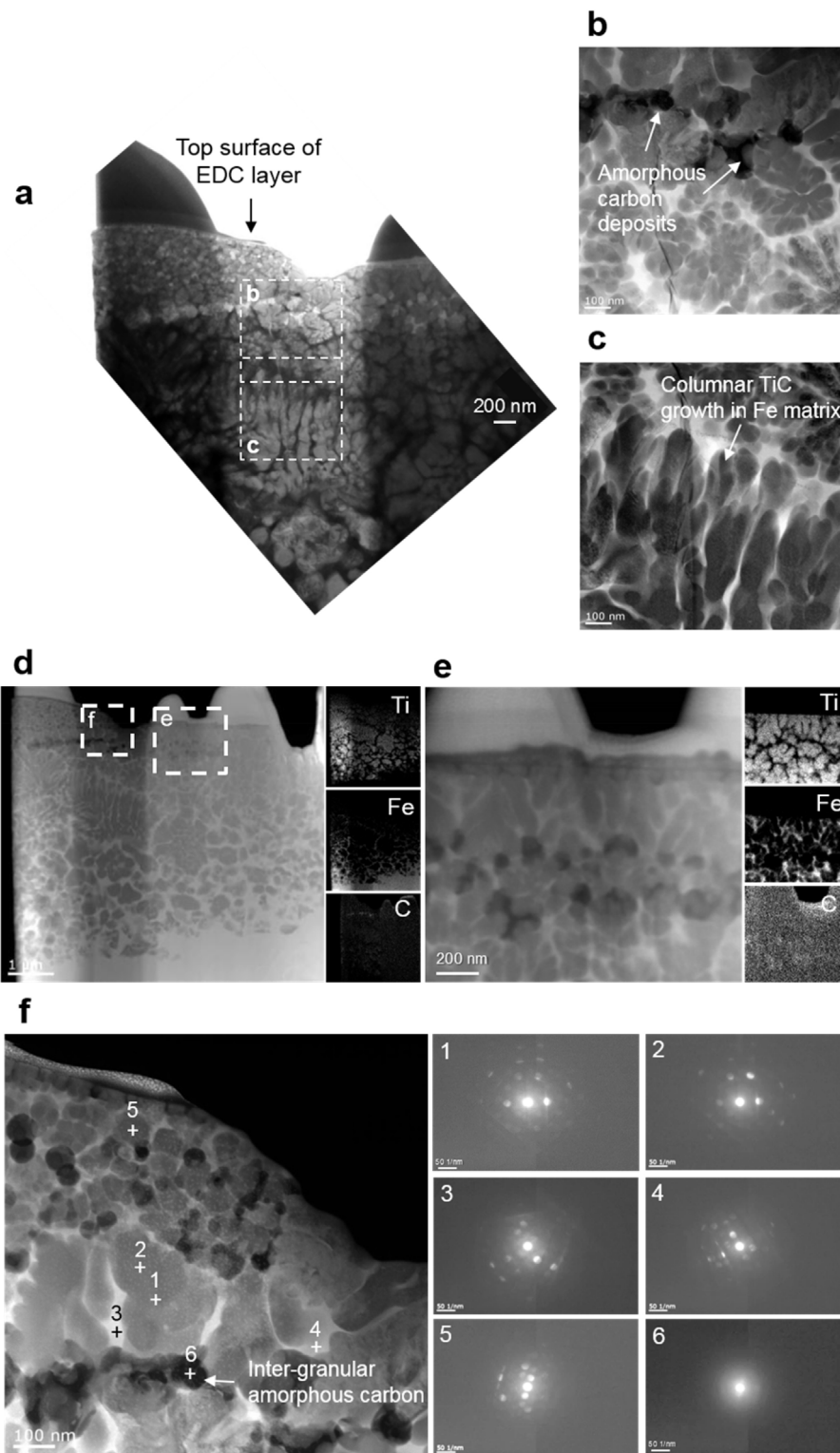
Fig. 4. (a) BF diffraction contrast TEM image of a continuum EDC TiC-Fe cermet coating in cross-section; (b,c) DF-STEM images of boxed regions showing transitional band and columnar growth microstructures; (d) Overview DF-STEM image of the coating with corresponding EDS maps; (e) DF-STEM image of the near surface region (boxed region in (d)) with corresponding EDS maps; (f) DF-STEM image of near surface (boxed region in (d)) with associated convergent beam electron diffraction (CBED) patterns from six different regions, as labelled in (f).

columnar grains towards the deposit/substrate interface, inter-mixed with some finer grains. Fig. 6(b:1–12) present SAED patterns through the depth of this deposit, acquired from the locations denoted in Fig. 6a. This data set is complemented by the EDS chemical maps shown in Fig. 6c and the EDS compositional data in Table 3,

acquired from the boxed regions of Fig. 6a(*i–iii*). It is noted that region *ii* corresponds to the largest TiC grain, with only a trace level of Fe being detected from the surrounding matrix. The Ga signal is an artefact, typical for sample foils prepared by FIB.
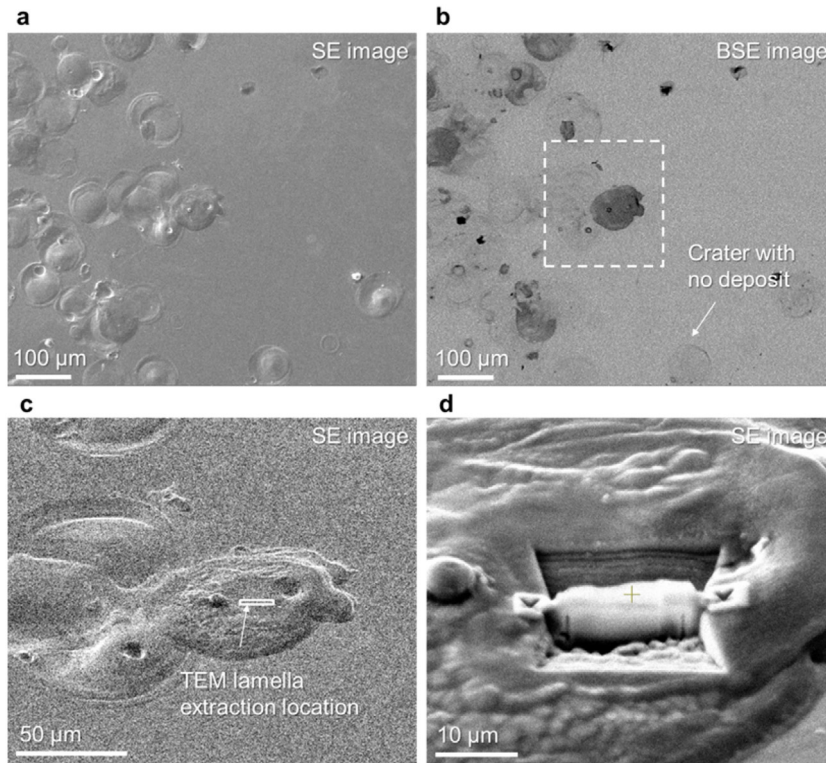
Fig. 5. Single deposit sample used for TEM sectioning: (a,b) SE and BSE images showing individual craters/deposits, EDC processed on 304 stainless steel; (c) magnified SE image of the boxed region in (b) showing location selected for sectioning; (d) SE image of FIB milled, electron transparent sample foil.
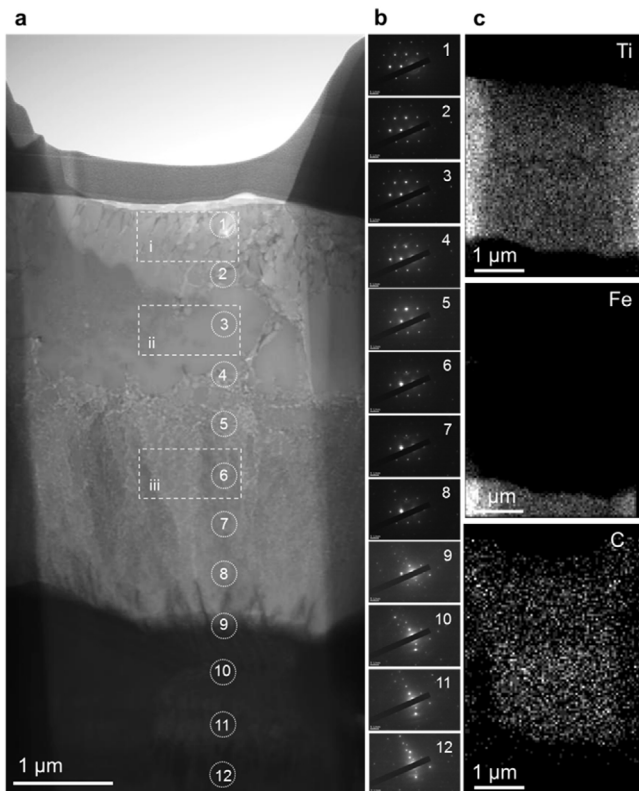

Fig. 6. (a) BF-STEM image of a single EDC processed deposit, in cross-section geometry; (b: 1–12) SAED patterns recorded sequentially through the deposit, as labelled in (a); and (c) Associated EDS maps for Ti, Fe and C.

It is evident that TiC is the dominant phase throughout the entire depth of this deposit. Further, the SAED patterns of Fig. 6(b:1–8) exhibit the same crystallographic projection, consistent with a dominance of single crystalline material. In practice, this means there is a high level of co-operative alignment of TiC grains throughout the deposit upon crystallisation from the melt pool and a single solidification front, emanating from the coating/substrate interface. The SAED patterns of Fig. 6(b:9–12) then indicate an abrupt transition into the bulk austenitic stainless steel substrate. The EDS data indicate a good level of compositional homogeneity of the deposit, with slightly enhanced levels of Fe and Cr in region *i*, nearest the surface. The significant enhancement of the C level near to the surface may be attributed to the incorporation of excess C from the cracked dielectric oil.

Fig. 7a,b are complementary bright field (BF) and dark field (DF) diffraction contrast TEM images, showing the interface between regions *ii* and *iii* of the deposit (Fig. 6a). Two slightly dis-oriented grains are shown, denoted A and B, with the DF image confirming the crystallographic alignment of Grain A material across this transition zone.

Fig. 8 presents a DF-STEM image highlighting fine scale structure in the vicinity of regions *i/ii* of Fig. 6a, with associated EDS maps confirming a distribution of Fe and enhanced levels of C surrounding the TiC grains. This is consistent with the phase separation of TiC of Fe from the melt upon rapid cooling to form the cermet.

Fig. 9a,b present STEM images of the columnar grain structure above the deposit/substrate interface, emphasising again a process of directional solidification during rapid cooling. Further, Fig. 9c,d present a complementary high magnification DF-STEM image and an EDS Fe map showing a distribution of Fe into the deposit, between the TiC grains, indicative of a process of capillary action.
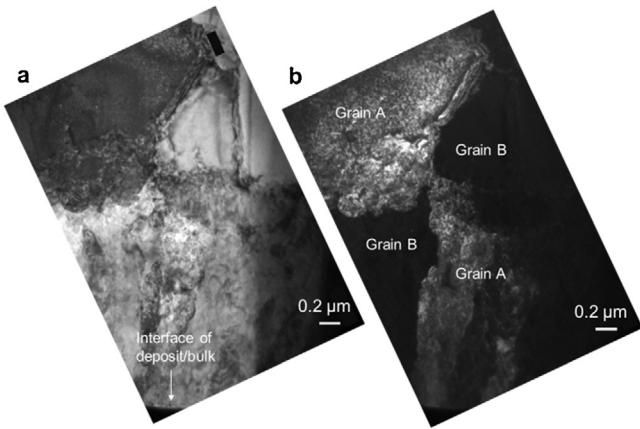
Fig. 7. Complementary (a) bright field and (b) dark field TEM images across the interface region ii/iii in Fig. 6a showing crystallographic alignment of grains across the boundary.

Fig. 8. DF-STEM image of transition region between i/ii of Fig. 6a and associated EDS maps showing a distribution of Fe and C between the TiC grains.

4. Discussion

This study has provided insights into the mechanisms of cermet coating development during conventional EDC processing of stainless steel using a TiC sacrificial tool electrode, through comparison of a single deposit with a continuum coating. When comparing the microstructure of a single deposit with that of a coating, it should be noted that the latter experienced ~200 sparks per location under the processing conditions used here. The number of sparks per location was estimated by the total number of sparks
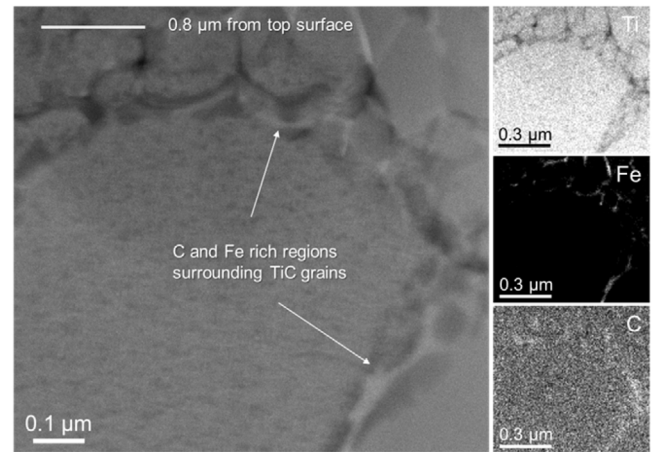
from the continuum processing multiplied by the area of influence of a single spark divided by the total area processed. Based on the following waveform data: the total time per spark comprised an on-time of 8 μs, an off-time of 256 μs and an ignition delay time of ~100 μs. Hence, a coating time of 30 min resulted in a total of ~5×10^6 sparks. The SE imaging of individual craters returned a mean diameter of ~70 μm. For a total coating area of 100 mm^2, this equates to ~200 sparks per location. In particular, the characterisation data provides direct evidence for the structure of these EDC processed materials following cooling of the melt pool. Accordingly,
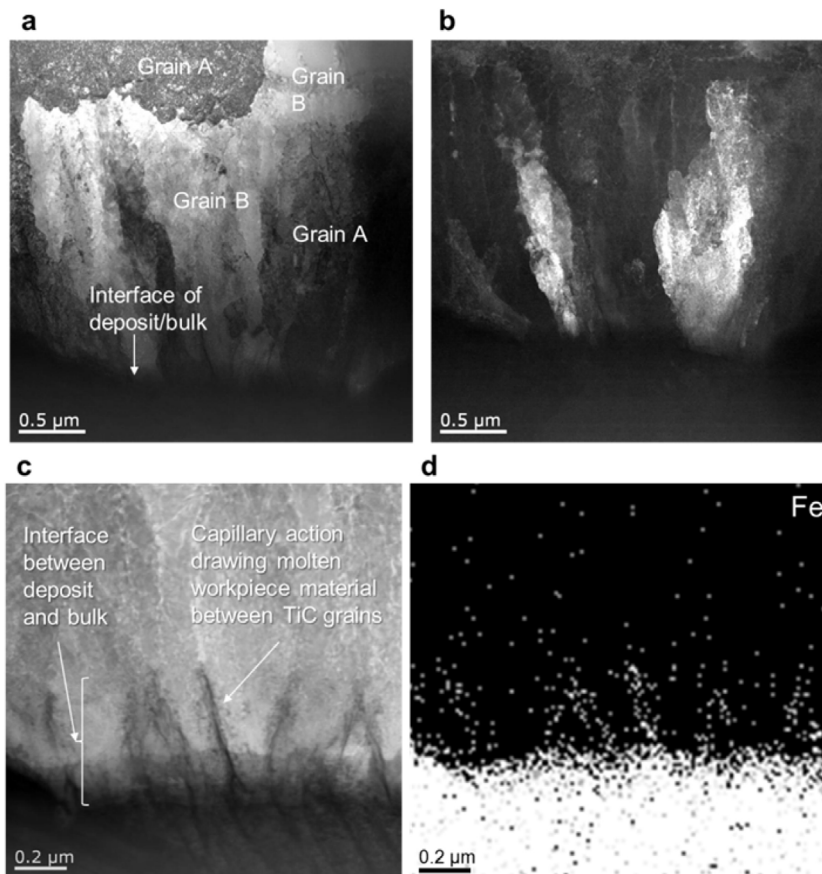

Fig. 9. (a,b) STEM images showing the columnar grain structure above the deposit/substrate interface and (c,d) high magnification DF-STEM image and EDS Fe map of the deposit/substrate interface showing the distribution of Fe between the TiC grains.
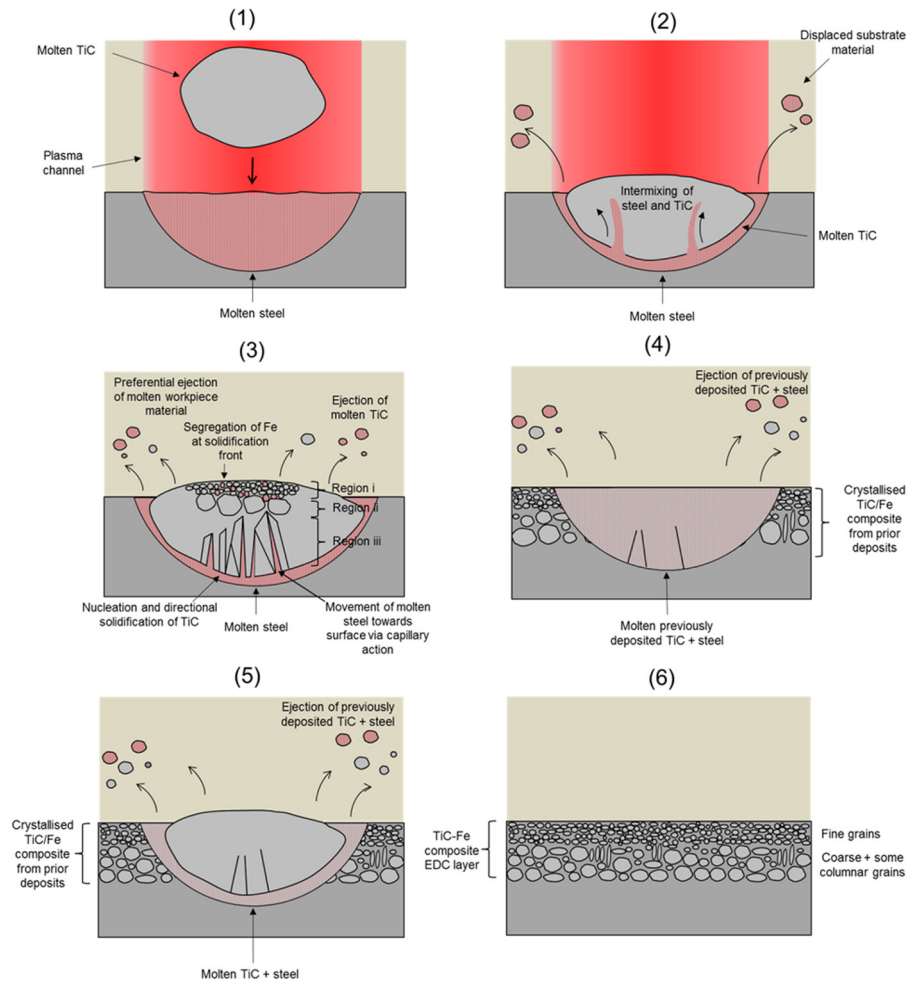
Fig. 10. Schematic representation of the EDC process, with the development of: (Steps 1–3) A single TiC dominated deposit; and (Steps 4–6) a continuum, intermixed TiC-Fe cermet coating.

Fig. 10 presents schematic diagrams summarising the key steps in the formation of an initial TiC deposit (Steps 1–3) and a developed continuum TiC-Fe cermet coating (Steps 4–6).

In Fig. 10, Steps 1 and 2, during discharge on-time, a molten particle of TiC is depicted fusing with a melt pool created at the workpiece surface beneath the plasma channel. Application of the Scherrer equation to the XRD data indicated that the TiC grains from the starting tool electrode exhibited average grain sizes on the scale of ~130 nm, being larger than the ~40 nm TiC average grain sizes within the coating (Algodi et al., 2016), being supported by Fig. 4f which demonstrates the development of ~40 nm sized grains near to the top surface, as sampled by XRD. This is consistent with the constituents of the melt pool being fully molten prior to solidification. Intermixing of workpiece material with TiC occurs during the melt pool lifetime. At the end of the initial discharge process, it is recognised that TiC will solidify before the Fe phase, given that the melting point of TiC (3430 K) is very much higher than the melting point of 304 stainless steel (1723 K). The concept of cermet phase separation is supported also by the Ti-C-Fe phase diagram (Ali Emamian et al., 2011). Hence, the initial solidified deposit becomes dominated strongly by TiC whilst substrate material is displaced preferentially due to its lower melting point. The thermal conductivity of the substrate (16.2 W/m-K) exceeds that of the dielectric oil (0.15 W/m-K) and hence it is considered that solidification progresses from the coating/substrate interface, promoted by conduction into the substrate. The initial development of TiC columnar grains (region iii) is followed by the nucleation

and growth of larger, and by implication, purer TiC grains at a slightly lower cooling rate (region ii). The final stage of smaller, more equiaxed TiC grain growth at the surface (region i) is consistent with solidification of the final part of the melt pool containing higher concentrations of elements from the substrate, as indicated by the EDS data, within which more heterogeneous nucleation sites would be available. A small remnant Fe volume fraction surrounding the TiC grains comprises the cermet matrix following complete solidification. There are three potential sources for C in this system, *i.e.* from the stainless steel substrate, the dielectric oil and the TiC. It is considered excess C in the system may originate from the oil and in combination with C from substrate contributes to the development of the trace levels of Fe_3C and Cr_3C_2 identified. The reaction of C with molten iron to form Fe_3C is a commonly reported phase present within EDM steels and hence is not a surprising result. It is known also that iron carbides can form during fast as well as slow cooling processes (Cabanillas et al., 2000).

The significantly higher concentration of Fe nearer the surface compared to the central regions of the deposit (Table 3) is consistent with the segregation of workpiece material ahead of the crystallisation front moving in the direction of the surface (Kuech, 2015). This mechanism is particularly valid in the case of the TiC-Fe system given the lack of solubility of Fe in TiC. Slightly higher Fe levels at the bottom of the deposit compared to its centre may be explained by capillary action during the final stages of solidification facilitated by grain shrinkage upon rapid cooling (see Fig. 9c,d). Such capillary action of the liquid steel phase between TiC particles is thought

to be a key densification mechanism in the processing of TiC-steel cermets by sintering (Wang et al., 2015) and self-propagating high temperature synthesis (SHS) (Wang et al., 2005).

It is recognised that material movement is constrained by the lifetime of the melt pool and it is considered that the deposit is solid prior to the next localised spark and melt pool formation event, which leads to progressive incorporation of more substrate and tool electrode material into the developing coating, by a repetition of these same intermixing and rapid solidification processes. Fig. 10, Steps 4 and 5, represent two intermediate stages of continuum coating development, with localised sparking events leading to next step melt pool formation, either with (5) or without (4) the successful incorporation of TiC. It is considered that the much higher boiling point of TiC will inhibit the ejection of the TiC from the melt pool via the boiling mechanism during and after discharge (Kunieda et al., 2005). However, when combined with the many sparking events which do not lead to TiC deposition, but simply localised remelting of the coating, this leads to a net dilution effect, *i.e.* promoted by sparking events without TiC incorporation. Hence, the sequence of many localised melt pool formation and solidification events results ultimately in the formation of a more Fe-rich, TiC-Fe cermet coating (Fig. 10, Step 6).

A number of insights are also provided from this data set relating to the development of EDC processed continuum coatings. For the processing conditions used here, the resultant TiC-Fe cermet exhibited a mean thickness of 8 μm, varying between 2 and 14 μm (Fig. 2c). This variability in coating thickness is attributed to a combination of deposit and crater overlap formations, along with non-uniform removal of material at the end of each sparking event. Clustering of sparking events, promoted by accumulations of debris due to gas bubble expansion upon plasma extinction (Kitamura et al., 2015), and non-uniformity of the tool electrode surface, resulting in variation in plasma properties may also contribute to this variability. Conversely, the range of TiC grain sizes and banded structures within the developed continuum cermet coating reflects simply the progression of the solidification front and localised cooling rates. It is considered unlikely that EDC can be used to create a pure coating, and that dilution of developing coating with substrate material is inevitable. The single TiC-rich deposit here contained a 2 wt% contribution of Fe at the surface, whilst the continuum TiC-Fe cermet coating contained ~30 wt% Fe. Hence, the dilution effect from repeated sparking suggests that time of processing is a critical EDC processing parameter, with an inherent risk of over-processing leading to the development of substrate-rich cermets.

5. Conclusions

EDC, using a sacrificial PM TiC tool electrode at negative polarity, has been used successfully to form a TiC-Fe cermet coating on stainless steel. An investigation of a single deposit and a continuum coating, processed under the same, standard EDC conditions, has provided insight into the generic principles of ED coating formation. SE imaging showed a continuum coating (30 wt% Fe) to comprise cellular deposits, bounded by cracks and voids, on the scale and distribution of individual sparking events, whilst XRD confirmed the presence of distinct phases of TiC and austenite/martensite, indicative of phase separation and rapid cool-down. Cross-sectional TEM demonstrated the presence of a complex, banded, grain structure exhibiting a mixture of equiaxed and columnar TiC grains, within an Fe-based matrix, along with some concentrations of C attributable to cracked dielectric oil. Investigation of a single deposit (2 wt% Fe) demonstrated the dominance of TiC with grain sizes very much smaller than those of the PM tool electrode, confirming the TiC deposit to be fully molten at the time of solidification. Further, the strong crystallographic alignment of grains, along with

a distinctive banded microstructure, provided evidence for a solidification front emanating from the coating/substrate interface with the enhancement of substrate material towards the surface. Filamentary incorporations of Fe from the substrate into the deposit, between the TiC grains, are indicative of a small amount of capillary action during the final stages of solidification. It is recognised that the continuum coating was formed following ~200 sparks per location, in this instance, using standard EDC processing conditions. It is considered that each sparking event remelts previously solidified material, with or without additional TiC incorporation, the combination of which leads to a gradual dilution of the melt pool and the formation of a TiC-Fe cermet coating with increasing levels of Fe. Accordingly, it has been shown that EDC may be used to form cermet coatings and hence is applicable to the development of hard to process ceramics. However, it is implicit that time of processing becomes a critical parameter for EDC in general, with an inherent possibility of over-processing leading to excessive dilution of the coating layer with substrate material.

References

S.J. Algodi, J.W. Murray, M.W. Fay, A.T. Clare, P.D. Brown, Electrical discharge coating of nanostructured TiC-Fe cermets on 304 stainless steel, Surf. Coat. Technol.

Emamian, Ali, Corbin, Stephen F., Khajepour, A., 2011. In-Situ Deposition of Metal Matrix Composite in Fe-Ti-C System Using Laser Cladding Process, Metal, Ceramic and Polymeric Composites for Various Uses. InTech.

Cabanillas, E.D., Desimoni, J., Punte, G., Mercader, R.C., 2000. Formation of carbides by electro-discharge machining of alpha iron. Mater. Sci. Eng.: A 276, 133–140.

Kitamura, T., Kunieda, M., Abe, K., 2015. Observation of relationship between bubbles and discharge locations in EDM using transparent electrodes. Precis. Eng. 40, 26–32.

Kuech, T.F., 2015. 21 – Metal organic vapor phase epitaxy chemical kinetics. In: Handbook of Crystal Growth, second edition. North-Holland, Boston, pp. 869–907.

Kumar Saxena, K., Suman Srivastava, A., Agarwal, S., 2016. Experimental investigation into the micro-EDM characteristics of conductive SiC. Ceram. Int. 42, 1597–1610.

Kunieda, M., Kobayashi, T., 2004. Clarifying mechanism of determining tool electrode wear ratio in EDM using spectroscopic measurement of vapor density. J. Mater. Process. Technol. 149, 284–288.

Kunieda, M., Lauwers, B., Rajurkar, K.P., Schumacher, B.M., 2005. Advancing EDM through fundamental insight into the process. CIRP Ann. Manuf. Technol. 54, 599–622.

Moro, T., Mohri, N., Otsubo, H., Goto, A., Saito, N., 2004. Study on the surface modification system with electrical discharge machine in the practical usage. J. Mater. Process. Technol. 149, 65–70.

Murray, J., Zdebski, D., Clare, A.T., 2012. Workpiece debris deposition on tool electrodes and secondary discharge phenomena in micro-EDM. J. Mater. Process. Technol. 212, 1537–1547.

Murray, J.W., Fay, M.W., Kunieda, M., Clare, A.T., 2013. TEM study on the electrical discharge machined surface of single-crystal silicon. J. Mater. Process. Technol. 213, 801–809.

Schumacher, B.M., 2004. After 60 years of EDM the discharge process remains still disputed. J. Mater. Process. Technol. 149, 376–381.

Suzuki, S., Kobayashi, S., 2013. Mechanisms of TiC layer formation on high speed steel by a single pulse in electrical discharge machining. Electrochim. Acta 114, 844–850.

Wang, H.Y., Jiang, Q.C., Ma, B.X., Wang, Y., Zhao, F., 2005. Reactive infiltration synthesis of TiB2–TiC particulates reinforced steel matrix composites. J. Alloys Compd. 391, 55–59.

Wang, Z., Lin, T., He, X., Shao, H., Zheng, J., Qu, X., 2015. Microstructure and properties of TiC-high manganese steel cermet prepared by different sintering processes. J. Alloys Compd. 650, 918–924.